NiFe layered double hydroxide electrodeposited on Ni foam coated with reduced graphene oxide for high-performance supercapacitors

Min Li, Roxana Jijie, Alexandre Barras, Pascal Roussel, Sabine Szunerits, Rabah Boukherroub

NiFe Layered Double Hydroxide Electrodeposited on Ni Foam Coated with Reduced Graphene Oxide for High-Performance Supercapacitors

Min Li,[1] Roxana Jijie,[1] Alexandre Barras,[1] Pascal Roussel,[2] Sabine Szunerits[1] and Rabah Boukherroub[1]

[1]*Univ. Lille, CNRS, Centrale Lille, ISEN, Univ. Valenciennes, UMR 8520 - IEMN, F-59000 Lille, France*

[2]*Univ. Lille, CNRS, ENSCL, Centrale Lille, Univ. Artois, UMR8181, UCCS-Unité de Catalyse et Chimie du Solide, Lille, F-59000, France*

Abstract

High-performance electrode materials consisting of intertwined caterpillar-like NiFe layered double hydroxide bridges coated on reduced graphene oxide modified Ni foam (NiFe LDHs/rGO/NF) were prepared *via* a facile two-step electrodeposition method. First, rGO was electrochemically coated onto NF at a constant potential of -1.2 V *vs.* SCE for 600 s. Then NiFe LDHs of different Ni to Fe ratios were electrodeposited onto the formed rGO/NF electrodes at -1.2 V *vs.* SCE for 10 s. Under optimized conditions, NiFe LDHs/rGO/NF composites displayed a high specific capacitance of 1462.5 F g^{-1} at a current density of 5 A g^{-1} and retained about 64.7% of the original capacitance after 2000 cycles. Furthermore, a flexible asymmetric supercapacitor was prepared using NiFe LDHs/rGO/NF as the cathode and mesoporous carbon (MC) coated on NF as the anode. The supercapacitor exhibited an energy density of 17.71 Wh kg^{-1} and a power density of 348.49 W kg^{-1}. All of these findings suggest that the new electrodes developed in this work hold a potential application prospect in flexible energy storage devices.

Keywords: *Ni-Fe LDHs; Nickel foam; Graphene; Electrodeposition; Flexible supercapacitors.*

*To whom correspondence should be addressed: rabah.boukherroub@univ-lille.fr (R. Boukherroub); Tel: +33 3 62 53 17 24; Fax: 33 3 62 53 17 01.

1. Introduction

Due to increasing global energy consumption and demands for the next-generation electronics, it is urgent to find a breakthrough in energy storage devices, such as rechargeable batteries and/or supercapacitors, to satisfy the future development of a low-carbon and sustainable economy [1-4]. Supercapacitors, as energy storage devices, have drawn considerable attention owing to their high power density, long cycling lifespan, fast charge-discharge speed and low cost of production [5-8]. According to energy storage mechanism, supercapacitors are divided into electrochemical double layer capacitors (EDLCs) that are based on the charge storage of adsorbed ions and pseudocapacitors that depend on charge storage involving fast surface redox reactions [9-11]. It is universally acknowledged that carbon materials including carbon nanotubes [12], carbon spheres [13] and reduced graphene oxide (rGO) [14], transition metal oxides/hydroxides including nickel oxide (NiO) [15], manganese dioxide (MnO_2) [16], titanium dioxide (TiO_2) [17] and layered double hydroxides (NiMn LDHs) [18], and conducting polymers such as polypyrrole [19], polythiophene [20], and PEDOT-PSS [21] are promising for supercapacitor electrode materials.

Among the materials mentioned above, layered double hydroxides (LDHs), with the general composition of $M^{2+}_{1-x}M^{3+}_{x}(OH)_2(A^{n-})_{x/n}\cdot mH_2O$, in which M^{2+} and M^{3+} are respectively the bivalent metal cations (typically Ni^{2+}, Co^{2+}, Cu^{2+}, Mg^{2+}, Mn^{2+}) and trivalent metal cations (typically Fe^{3+}, Al^{3+}, V^{3+}, Cr^{3+}), A^{n-} is the interlayer anions (typically CO_3^{2-}, NO_3^-, OH^-), $x = M^{3+}/(M^{2+} + M^{3+})$, have evoked great attention for potential applications in catalysis, anion exchange materials, fire retardant materials and pseudocapacitors owing to their well-defined redox behavior and high redox activity [22-25]. For example, Li *et al*. synthesized hierarchical NiAl LDH nanotubes by integrating an atomic layer deposition (ALD) technique with a simple hydrothermal treatment for high performance supercapacitors [26]. Liu *et al*. prepared 2D hierarchical NiO/NiMn-LDH nanosheet arrays for supercapacitors with a high specific capacitance of 937 F g^{-1} at 0.5 A g^{-1} [27]. Even though high specific capacitance values are reported, the low electrical conductivity of LDHs hinders their potential application for electrochemical supercapacitors [28]. Thus, assembling LDHs with conductive materials will be an effective method to improve the electrical conductivity of the electrodes. For instance, nickel foam (NF) possesses next to good electrical properties, efficient electron transfer, high physical strength with an acceptable surface area and 3-dimensional (3D)

macro-porous structure, which are advantageous for high performance devices [11].

Herein, we prepared new 3D composite materials by combining NiFe LDHs and NF (NiFe LDHs/NF) *via* a facile and eco-friendly electrochemical method. Fe^{3+} was employed in the LDH composites, because compared to most metals such as cobalt and aluminum, iron is much cheaper and more abundant. To improve the conductivity of the electrode material, NF was electrochemically coated with reduced graphene oxide (rGO) prior to NiFe LDHs electrodeposition. Consequently, the obtained NiFe LDHs/rGO/NF composites exhibited excellent supercapacitor performance with a specific capacitance of 1462.5 F g^{-1} at a current density of 5 A g^{-1}. Hence, a flexible asymmetric supercapacitor was prepared using NiFe LDHs/rGO/NF as the cathode and mesoporous carbon (MC) coated on NF as the anode, displaying an energy density of 17.71 Wh kg^{-1} and a power density of 348.49 W kg^{-1}.

2. Experimental section

2.1. Materials and reagents

$Ni(NO_3)_2 \cdot 6H_2O$, $Fe(NO_3)_3 \cdot 9H_2O$, mesoporous carbon (MC) and graphite were obtained from Sigma-Aldrich (France). Nickel foam (NF) was purchased from Jiayisheng Company (China).

The water used throughout the experiments was purified with a Milli-Q system from Millipore Co. (resistivity = 18 MΩ.cm).

2.2. Preparation of graphene oxide (GO)

Graphene oxide (GO) was synthesized by the improved Hummers' method [29]. Typically, to a mixture of graphite flakes (1 g) and $KMnO_4$ (6 g) was added a 9:1 (volume) mixture of concentrated H_2SO_4/H_3PO_4 (40:13.3 mL) and allowed to react at about 50 °C under continuous stirring for 12 h. The reaction was cooled to room temperature, followed by adding ice (~100 mL) and 1 mL of 30% H_2O_2. Then, the mixture was centrifuged at 4500 rpm for 40 min, washed successively with 200 mL of 30% HCl, 200 mL of water, and 200 mL of ethanol. Finally, the obtained precipitate was vacuum-dried at room temperature.

2.3. Preparation of NiFe LDHs/NF

NiFe LDHs were electrochemically deposited onto the surface of nickel foam (NF) using different molar ratios: 5:0, 4:1, 3:2, 1:1, 2:3, 1:4, 0:5 of $Ni(NO_3)_2 \cdot 6H_2O$ and $Fe(NO_3)_3 \cdot 9H_2O$; the overall

molar concentration was 50 mM. Nickel foam (NF) acts as the working electrode; the counter electrode and the reference electrode are platinum foil and saturated calomel electrode (SCE), respectively. Typically, the potentiostatic deposition was performed at -1.2V *vs.* SCE for 10 s to form NiFe LDHs/NF. Different NiFe LDHs/NF electrodes were successfully prepared and samples with different $Ni(NO_3)_2 \cdot 6H_2O$ and $Fe(NO_3)_3 \cdot 9H_2O$ molar ratios of 5:0, 4:1, 3:2, 1:1, 2:3, 1:4, 0:5 were represented by S_0, S_1, S_2, S_3, S_4, S_5, S_6, respectively. All the synthesized samples were washed with water and ethanol, and further dried at 60 ^oC for 6 h.

2.4. Preparation of reduced graphene oxide coated nickel foam (rGO/NF)

To improve the conductivity of the electrode, reduced graphene oxide (rGO) was first coated on NF by the electrodeposition method. Typically, a 0.1 M $LiClO_4$ aqueous solution containing 1.5 mg mL^{-1} of graphene oxide (GO) was used as the electrolyte for graphene electrodeposition to obtain the rGO/NF. The deposition of reduced graphene oxide (rGO) was carried out by a potentiostatic method at a constant potential of -1.2 V *vs.* SCE for 600 s. Then, the resulting black sample was washed with water for several times.

2.5. Preparation of NiFe LDHs/rGO/NF

A two-step electrodeposition process was used to synthesize the NiFe LDHs/rGO/NF. First, rGO/NF was prepared using the same method mentioned above, followed by NiFe LDH electrodeposition using $Ni(NO_3)_2 \cdot 6H_2O$ and $Fe(NO_3)_3 \cdot 9H_2O$ at a molar ratio of 1:4 under constant potential of -1.2 V *vs.* SCE for 10 s to produce NiFe LDHs/rGO/NF, represented by S_7. Additionally, S_8 and S_9 were also prepared using different deposition times of 20 s and 30 s, respectively.

2.6. Characterization

Scanning electron microscopy (SEM) images were obtained using an electron microscope ULTRA 55 (Zeiss) equipped with a thermal field emission emitter and three different detectors (EsB detector with filter grid, high-efficiency In-lens SE detector, Everhart-Thornley secondary electron detector). The chemical composition of the electrode materials was analysed using X-ray photoelectron spectroscopy (XPS) (ESCALAB 220 XL spectrometer from Vacuum Generators featuring a monochromatic Al Kα X-ray source at 1486.6 eV).

2.7. Electrochemical measurements

All electrochemical measurements were conducted in a classical three electrode configuration cell containing 2 M KOH aqueous solution as the electrolyte using an electrochemical workstation (Autolab, Methrom) at ambient temperature. NiFe LDHs/rGO/NF was employed as the working electrode. A platinum foil and a saturated calomel electrode (SCE) acted as the counter electrode and reference electrode, respectively

Cyclic voltammetry (CV) curves were recorded in the potential range from 0 to +0.5 V at different scan rates between 10 and 200 mV s^{-1}. Galvanostatic charge-discharge (GCD) measurements were acquired at current densities from 5 to 30 A g^{-1}. Electrochemical impedance spectroscopy (EIS) was performed in the frequency range from 100 kHz to 0.01 Hz. The durability tests were performed by repeating 2000 charge-discharge cycles at a constant current density of 15 A g^{-1}.

2.8. Fabrication of an asymmetric supercapacitor

An asymmetric supercapacitor device was assembled using as-prepared NiFe LDHs/rGO/NF (S_7, 1 cm×1 cm) as the cathode and mesoporous carbon (MC)/NF as the anode, with the separator consisting of a filter paper soaked into 2 M KOH solution for 30 min. The MC/NF electrode consisted of active materials, carbon black and polyvinylidene difluoride (PVDF) in a mass proportion of 7:2:1, which was pasted on the nickel foam.

Electrochemical characterization was performed in a two-electrode system. The charge stored (Q) is determined following the equation (1):

$$Q = C \times m \times \Delta V \qquad (1)$$

$$C = \frac{I \times \Delta t}{m \times \Delta V} \qquad (2)$$

where C (F g^{-1}) is the specific capacitance, I (A) is the discharge current; Δt (s) is the discharge time, m (g) is the mass of active material and ΔV (V) is the potential window of discharge.

To acquire the optimal performance of the asymmetric supercapacitor, a charge balance Q_+ (charges stored in the positive electrode) = Q_- (charges stored in the negative electrode) between the two

electrodes is necessary so that the mass balancing follows the equation (3):

$$\frac{m_+}{m_-} = \frac{C_-\Delta V_-}{C_+\Delta V_+} \quad (3)$$

where m_+ and m_- are the mass of positive and negative electrode materials, respectively, C_+ and C_- are the specific capacitance of the positive and negative electrodes, respectively and ΔV_+ and ΔV_- are the potential window of the positive and negative electrodes, respectively.

The energy density (E, Wh kg^{-1}) and power density (P, W kg^{-1}) of the asymmetric supercapacitor can be calculated from the specific capacitance using the following equations:

$$E = \frac{0.5C \times \Delta V^2}{3.6} \quad (4)$$

$$P = \frac{E \times 3600}{\Delta t} \quad (5)$$

where C (F g^{-1}) is the specific capacitance, ΔV (V) is the potential window of discharge, Δt (s) is the discharge time.

3. Results and discussion

The procedure for the preparation of NiFe LDHs on reduced graphene oxide coated nickel foam (rGO/NF) is depicted in **Scheme 1**. NiFe LDHs/rGO/NF composites were successfully prepared through electrodeposition method. Graphene oxide (GO) was first electrochemically reduced into rGO under a constant potential of -1.2 V *vs.* SCE for 600 s, followed by the uniform deposition of the NiFe LDHs on rGO/NF at 4:1 molar ratios of $Ni(NO_3)_2$•$6H_2O$ and $Fe(NO_3)_3$•$9H_2O$. Similarly, NiFe LDHs with different molar ratios of $Ni(NO_3)_2$•$6H_2O$ and $Fe(NO_3)_3$•$9H_2O$ (5:0, 4:1, 3:2, 1:1, 2:3, 1:4, 0:5) were electrochemically deposited onto the surface of NF in absence of rGO.

Scheme 1.

The SEM images indicate that NiFe LDHs/NF obtained at different precursor ratios have similar morphologies (**Fig. 1** and **Fig. S1**). In the absence of Fe^{3+}, the as-obtained $Ni(OH)_2$ consists of a monolayer of nanosheets. With the increase of Fe^{3+} concentration, NiFe LDHs loading on the NF becomes denser, most likely due to partial replacement of Ni^{2+} by Fe^{3+}, which can restrain the self-aggregation of double hydroxide layers by electrostatic interaction and leads to an expansion in the dimension along layer stacking direction, yielding a high dispersion of Ni unit and denser nanosheets of the samples [28]. At the same time, for NiFe LDHs, we can regard it as Fe-doped $Ni(OH)_2$ composites, and it can significantly modulate the nanosheet morphology to increase the active surface area, boost more active sites and augment the intrinsic activity by tuning the electronic structure of $Ni(OH)_2$. And from the SEM images of these composites we can see that there existed the different synergy between the two metal ions with different ratio of Ni^{2+} and Fe^{3+}. In particular, when the molar ratio of Ni and Fe precursors is 1:4 (**Fig. 1b**), intertwined caterpillar-like NiFe LDHs bridges on NF appear, consisting of lots of nanosheets, which could act as a reservoir and shorten the ion transport distance. Additionally, the interconnected skeletons ensure more superficial electroactive species and preferential electrolyte ion transport. As illustrated in **Fig. 1c**, $Fe(OH)_3$ (NiFe LDHs without Ni precursor) is also an interlaced bridge; however, its structure is more tight and there are no decorated nanosheet branches. For the NiFe LDH/rGO/NF, rGO was successfully deposited on the NF prior to NiFe LDHs electrodeposition (**Fig. 1d**). The presence of rGO could further facilitate the electron transport and provide a better charge transfer kinetics and an enhanced electrochemical capacity [30].

Figure 1

X-ray photoelectron spectroscopy (XPS) survey scan confirmed the existence of both Ni_{2p} and Fe_{2p} elements in NiFe LDHs/NF (**Fig. S2**) and NiFe LDHs/rGO/NF (**Fig. 2a**) along with O_{1s} and C_{1s}. The presence of C_{1s} in NiFe LDHs/NF originates from surface contamination during sample handling. The C_{1s} high-resolution survey spectrum (**Fig. S2b**) of NiFe LDH/NF displays two types of

carbons: C=C (284.7 eV) and C=O (288.5 eV), while there are three types of carbons: C=C (284.7 eV), C-O (285.6 eV) and C=O (288.5 eV) for LDHs/rGO/NF (**Fig. 2b**). At the same time, the C content in NiFe LDHs/NF is lower than that of LDHs/rGO/NF, which further confirms that rGO was deposited on the surface of NF in LDHs/rGO/NF and the functional groups of GO were partially removed upon electrochemical reduction [31-33]. The Ni_{2p} high resolution XPS spectrum shows two peaks located at binding energies of 855.4 and 873.2 eV due to $Ni_{2p3/2}$ and $Ni_{2p1/2}$ of $Ni(OH)_2$, respectively, along with two satellite peaks (**Fig. 2c** & **Fig. S2c**) [34, 35].

Figure 2

The high-resolution spectrum of Fe_{2p} reflects that Fe species are mostly in their Fe^{3+} oxidation state (**Fig. S2d** & **Fig. 2d**), with two prominent peaks at 712.2 ($Fe_{2p3/2}$) and 725.4 eV ($Fe_{2p1/2}$) [36-38]. The high resolution XPS spectrum of the O_{1s} (**Fig. S3**) shows a single peak ascribed to -OH groups, further confirming that Ni and Fe are in the form of $Ni(OH)_2$ and $Fe(OH)_3$, respectively [38].

Raman spectroscopy is a valuable tool for analysis of carbon-based materials. **Figure S4** depicts the Raman spectrum of rGO/Ni composite. It comprises two peaks at 1353 and 1596 cm^{-1} due to the D- and G-bands of rGO, respectively. The presence of these characteristic graphitic bands confirms the successful electrodeposition of rGO on the Ni foam. The Raman spectrum of NiFe LDH/rGO/NF reveals the characteristic D-band (1355 cm^{-1}) and G-band (1603 cm^{-1}) of rGO along with new peaks at 328, 478, 567 and 691 cm^{-1} due to the vibration modes of NiFe LDH [39-41]. Interestingly, the D- and G-ands of rGO in NiFe LDH/rGO/NF are red-shifted, suggesting a strong interaction between rGO and NiFe LDH/NF.

The electrochemical properties of the samples were assessed in a classical three electrode configuration in 2 M KOH aqueous electrolyte by means of CV, GCD and EIS tests. **Fig. 3a** and **Fig. 3b** depict the CV curves of NiFe LDHs/NF and all the samples exhibited redox peaks due to Ni (II)/Ni(III) in the hydroxide sheets of NiFe LDHs, indicating that the capacitance characteristics are mainly due to Faradaic pseudocapacitance corresponding to the electrochemical reaction as follows:

$$Ni(OH)_2 + OH^- \leftrightharpoons NiOOH + H_2O + e^- \qquad (6)$$

Figure 3

The CV curves (**Fig. 3b**) indicate that the peak current of NiFe LDH 1:4 (S_5) electrode increases without a significant change of the curve shape, and the peak potential shifts as the scan rate increases, which originates from the increased internal resistance under higher scan rates. From **Fig. 3c**, we can see that NiFe LDH 1:4 (S_5) has the best performance with the longest discharge time. According to equation (2), the specific capacitance of NiFe LDH 1:4 (S_5) is determined to be 1325 F g^{-1} at a current density of 5 A g^{-1}. It is worth noting that NiFe LDH 0:5 (S_6) possesses a relatively higher specific capacitance than NiFe LDH 3:2 (S_2), NiFe LDH 1:1 (S_3) and NiFe LDH 2:3 (S_4), most likely due to the unique 3D bridge structure, as shown in **Fig. 1c**.

The calculated specific capacitance values of the electrodes from the galvanostatic charge-discharge (GCD) curves at different current densities are displayed in **Fig. 3d** and **Table 1**, confirming the good performance for all the samples. The specific capacitance values for NiFe LDH 1:4 (S_5) were calculated to be 1250, 1200, 1150 and 1050 F g^{-1} at the current densities of 10, 15, 20 and 30 A g^{-1}, respectively.

Table 1. Specific capacitance (F g^{-1}) of the NiFe LDHs/NF electrodes.

Current density (A g^{-1}) / Samples	5	10	15	20	30
$Ni(OH)_2$ (**S_0**)	700	650	600	550	525
NiFe LDH 4:1 (**S_1**)	1075	1000	900	800	675
NiFe LDH 3:2 (**S_2**)	550	450	375	350	300
NiFe LDH 1:1 (**S_3**)	625	610.44	600	575	525
NiFe LDH 2:3 (**S_4**)	612.5	525	487.5	400	375
NiFe LDH 1:4 (**S_5**)	1325	1250	1200	1150	1050
$Fe(OH)_3$ (**S_6**)	975	825	750	700	675

EIS measurements, performed in the frequency range from 100 kHz to 0.01 Hz in 2 M KOH (**Fig. S5**), revealed that the Nyquist plots are similar in shape and comprise a small semicircle at high

frequency region and a slope line (Warburg curve) in the low frequency region. Among them, for the sample NiFe LDH 1:4 (S_5), the R_s related to the internal resistance of an electrode material, electrolyte resistance and contact resistance between the active material and substrate was determined to be 1.91 ohm cm^2, and R_{ct} (charge transfer resistance) value was 24.23 ohm cm^2. Due to its unique characteristics, such as large specific surface area, high electrical conductivity and chemical stability, graphene has been widely employed in supercapacitors. In order to improve the performance of the electrodes, NiFe LDHs/rGO/NF (S_7) was prepared using a two-step electrodeposition according to the process in **Scheme 1**. The electrochemical impedance spectra of NiFe LDHs/NF (S_5) and NiFe LDHs/rGO/NF (S_7) are depicted in **Fig. 4a** the inset corresponds to the equivalent circuit for impedance analysis based on characterization by the software of ZSimDemo3.30d, where R_s is the internal resistance, R_{ct} is the charge-transfer resistance, C_{dl} is the double-layer capacitance, W_o is the Warburg element. It can be clearly seen that NiFe LDHs/rGO/NF (S_7) has a smaller R_s (1.072 ohm cm^2), a combination of the contact resistance of the active material with the substrate and the test cell to the apparatus, the ionic resistance of the electrolyte, and the intrinsic resistance of the electrode. The sample has also a lower R_{ct} (13.48 ohm cm^2). It is likely that rGO provides easy electron-transfer access and more Fe^{3+} ions enhanced the electrical conductivity of $Ni(OH)_2$ [37]. **Fig. 4b** indicates that both NiFe LDHs/NF and NiFe LDHs/rGO/NF possess good rate capability. Upon increasing the current density from 5 to 30 A g^{-1}, about 79% of NiFe LDHs/NF specific capacitance is retained, while 72 % capacitance is retained for NiFe LDHs/rGO/NF. Finally, the prepared electrodes are subjected to an extended charge–discharge cycling at 15 A g^{-1} (**Fig. 4c**). After 2000 cycles, 47% and 64.7% of the original capacitance is retained for NiFe LDH/NF and NiFe LDHs/rGO/NF electrodes, respectively. At the same time, the electrochemical properties of the prepared samples were measured using the same method. Compared with NiFe LDHs/NF 1:4 (S_5), NiFe LDHs/rGO/NF 20 s (S_8) and NiFe LDHs/rGO/NF 30 s (S_9), NiFe LDHs/rGO/NF (S_7) possessed the larger discharging currents with obviously a pair of characteristic redox peaks in the CV, as shown in **Fig. 4d** and **Fig. S6**. At different scan rates, we could observe the changes of anodic and cathodic peaks towards more positive and negative directions in **Fig. 4e**, originating from the increased internal resistance under higher scan rates. Furthermore, as seen in **Fig. 4f** NiFe LDHs/rGO/NF (S_7) exhibits a better performance and its specific capacitance increased to 1462.5 F g^{-1}.

Figure 4

Fig. 5a schematically illustrates an asymmetric supercapacitor device, in which the as-obtained NiFe LDH/rGO/NF works as the cathode and mesoporous carbon/nickel foam (MC/NF) acts as the anode by packing them between two PET films. As illustrated in **Fig. 5b**, the flexible NiFe LDH/rGO/NF//MC asymmetric supercapacitor possesses a great potential window (up to 1.6 V), which is attributed to the great potential window of MC (**Fig. S7**); the CVs display similar shapes, indicating an excellent capacitive performance. **Fig. 5c** depicts the CV curves of the asymmetric supercapacitor obtained at different scan rates in the potential window between 0 and +1.6 V, exhibiting an excellent capacitance behavior. As we can see from **Fig. 5e**, the initial specific capacitance values were 65.07, 35.93, 19.89, 17.83 and 17.49 F g^{-1} at different current densities of 0.5, 0.8, 1, 2 and 3 A g^{-1}, corresponding to the discharging curves shown in **Fig. 5d**. An equivalent circuit for impedance analysis of the asymmetric supercapacitor is illustrated in **Fig. 5f**, in which R_s is the internal resistance, R_{ct} is the charge-transfer resistance, C_{dl} is the double-layer capacitance, W_o is the Warburg element, C_l is the low-frequency mass capacitance. We can also see that the Nyquist plot exhibits a semicircle associated with the charge transfer resistance at the high-frequency range and a sloping line at the low-frequency region. From the inset in **Fig. 5f**, the R_s and R_{ct} values are estimated to be about 12.3 and 19.4 ohm cm^2, respectively.

Figure 5

To assess the electrochemical performance of the as-fabricated asymmetric supercapacitor, the Ragone plots, according to equations (4) and (5), are generated in **Fig. 5g**. The results demonstrate that the asymmetric supercapacitor device reached a high energy density of 17.71 Wh kg^{-1} at a power density of 348.49 W kg^{-1}. These values are greater than that of CoMn-LDH/AC asymmetric supercapacitor [23], MnO_2/AC asymmetric supercapacitor [42], MnO_2/P-GA asymmetric supercapacitor [43], PPy/rGO/NCs asymmetric supercapacitor [44], Cu_2O/CuO/Co_3O_4//AG asymmetric supercapacitor [45], Ni-Co oxide/AC asymmetric supercapacitor [46] and $MnFe_2O_4$/$LiMn_2O_4$ asymmetric supercapacitor [47]. Furthermore, the mechanical properties and flexibility of the asymmetric supercapacitor device were evaluated (**Fig. 5h**). There is no obvious

change in the CV curves at different bending angles, indicating a satisfactory flexible performance of the asymmetric supercapacitor.

4. Conclusions

In conclusion, new 3D intertwined caterpillar-like composite materials were prepared by combining NiFe LDHs with different Ni^{2+} and Fe^{3+} molar ratios and nickel foam (NiFe LDHs/NF) using an eco-friendly and facile electrochemical method. The NiFe LDH/NF with Ni^{2+} and Fe^{3+} molar ratio = 1:4 achieved excellent supercapacitor performance with a high capacitance value of 1325 F g^{-1} at a current density of 5 A g^{-1}. To further improve the conductivity of the NiFe LDHs/NF electrodes, NiFe LDHs/rGO/NF composites were synthesized using a two-step electrodeposition method. Consequently, NiFe LDHs/rGO/NF composites exhibited improved performance with a specific capacitance of 1462.5 F g^{-1} at a current density of 5 A g^{-1}. Additionally, a capacitance retention of 64.7% after 2000 cycles was recorded, suggesting a good stability of the electrode material. Moreover, a flexible asymmetric supercapacitor was prepared using NiFe LDHs/rGO/NF as the cathode and mesoporous carbon coated on nickel foam (MC/NF) as the anode; the device displayed an energy density of 17.71 Wh kg^{-1} at a power density of 348.49 W kg^{-1}, suggesting a promising potential in supercapacitor applications.

Acknowledgements

The authors gratefully acknowledge financial support from the Centre National de la Recherche Scientifique (CNRS), the University of Lille – Sciences and Technologies, the Hauts-de-France region. Min Li thanks Chinese government for the China Scholarship Council fellowship.

References

[1] Z. Gao, C. Bumgardner, N. Song, Y. Zhang, J. Li, X. Li, Cotton-textile-enabled flexible self-sustaining power packs via roll-to-roll fabrication, Nature Commun. 7 (2016) 11586.
[2] Z. Li, M. Shao, L. Zhou, R. Zhang, C. Zhang, J. Han, M. Wei, D.G. Evans, X. Duan, A flexible all-solid-state micro-supercapacitor based on hierarchical CuO@layered double hydroxide core–shell nanoarrays, Nano Energy 20 (2016) 294-304.
[3] Y. Wang, Y. Song, Y. Xia, Electrochemical capacitors: mechanism, materials, systems, characterization and applications, Chem. Soc. Rev. 45 (2016) 5925-5950.
[4] X. Liu, A. Zhou, T. Pan, Y. Dou, M. Shao, J. Han, M. Wei, Ultrahigh-rate-capability of a layered double hydroxide supercapacitor based on a self-generated electrolyte reservoir, J. Mater. Chem. A 4 (2016) 8421-8427.

[5] S.C. Sekhar, G. Nagaraju, J.S. Yu, Conductive silver nanowires-fenced carbon cloth fibers-supported layered double hydroxide nanosheets as a flexible and binder-free electrode for high-performance asymmetric supercapacitors, Nano Energy 36 (2017) 58-67.
[6] S. Li, C. Yu, J. Yang, C. Zhao, M. Zhang, H. Huang, Z. Liu, W. Guo, J. Qiu, A superhydrophilic "nanoglue" for stabilizing metal hydroxides onto carbon materials for high-energy and ultralong-life asymmetric supercapacitors, Energy Environm. Sci. 10 (2017) 1958-1965.
[7] X. Liu, C. Wang, Y. Dou, A. Zhou, T. Pan, J. Han, M. Wei, A NiAl layered double hydroxide@carbon nanoparticles hybrid electrode for high-performance asymmetric supercapacitors, J. Mater. Chem. A 2 (2014) 1682-1685.
[8] X. Xiong, D. Ding, D. Chen, G. Waller, Y. Bu, Z. Wang, M. Liu, Three-dimensional ultrathin Ni(OH) 2 nanosheets grown on nickel foam for high-performance supercapacitors, Nano Energy 11 (2015) 154-161.
[9] F. Li, Y.X. Zhang, M. Huang, Y. Xing, L.L. Zhang, Rational Design of Porous MnO_2 Tubular Arrays via Facile and Templated Method for High Performance Supercapacitors, Electrochim. Acta 154 (2015) 329-337.
[10] C.-T. Hsu, C.-C. Hu, Synthesis and characterization of mesoporous spinel $NiCo_2O_4$ using surfactant-assembled dispersion for asymmetric supercapacitors, J. Power Sources 242 (2013) 662-671.
[11] M. Li, M. Zhou, Z.Q. Wen, Y.X. Zhang, Flower-like NiFe layered double hydroxides coated MnO 2 for high-performance flexible supercapacitors, J. Energy Storage 11 (2017) 242-248.
[12] Y. Zhu, K. Shi, I. Zhitomirsky, Polypyrrole coated carbon nanotubes for supercapacitor devices with enhanced electrochemical performance, J. Power Sources, 268 (2014) 233-239.
[13] Y. Zhang, M. Dong, S. Zhu, C. Liu, Z. Wen, MnO_2@colloid carbon spheres nanocomposites with tunable interior architecture for supercapacitors, Mater. Res. Bull. 49 (2014) 448-453.
[14] L. Gurusamy, S. Anandan, J.J. Wu, Synthesis of Reduced Graphene Oxide Supported Flower-like Bismuth Subcarbonates Microsphere ($Bi_2O_2CO_3$-RGO) for Supercapacitor Application, Electrochim. Acta 244 (2017) 209-221.
[15] H. Xiao, F. Qu, X. Wu, Ultrathin NiO nanoflakes electrode materials for supercapacitors, Appl. Surf. Sci. 360 (2016) 8-13.
[16] H. Chen, X.L. Liu, J.M. Zhang, F. Dong, Y.X. Zhang, Rational synthesis of hybrid $NiCo_2S_4$ @MnO_2 heterostructures for supercapacitor electrodes, Ceram. Int. 42 (2016) 8909-8914.
[17] S.S. Raut, G.P. Patil, P.G. Chavan, B.R. Sankapal, Vertically aligned TiO_2 nanotubes: Highly stable electrochemical supercapacitor, J. Electroanal. Chem. 780 (2016) 197-200.
[18] X.L. Guo, J.M. Zhang, W.N. Xu, C.G. Hu, L. Sun, Y.X. Zhang, Growth of NiMn LDH nanosheet arrays on KCu_7S_4 microwires for hybrid supercapacitors with enhanced electrochemical performance, J. Mater. Chem. A 5 (2017) 20579-20587.
[19] Y. Huang, M. Zhu, Y. Huang, H. Li, Z. Pei, Q. Xue, Z. Liao, Z. Wang, C. Zhi, A modularization approach for linear-shaped functional supercapacitors, J. Mater. Chem. A 4 (2016) 4580-4586.
[20] R.B. Ambade, S.B. Ambade, N.K. Shrestha, Y.C. Nah, S.H. Han, W. Lee, S.H. Lee, Polythiophene infiltrated TiO_2 nanotubes as high-performance supercapacitor electrodes, Chem. Commun. 49 (2013) 2308-2310.
[21] Y. Hou, Y. Cheng, T. Hobson, J. Liu, Design and synthesis of hierarchical MnO_2 nanospheres/carbon nanotubes/conducting polymer ternary composite for high performance electrochemical electrodes, Nano Lett. 10 (2010) 2727-2733.

[22] P. Guoxiang, X. Xinhui, L. Jingshan, C. Feng, Y. Zhihong, F. Hongjin, Preparation of CoAl layered double hydroxide nanoflake arrays and their high supercapacitance performance, Appl. Clay Sci. 102 (2014) 28-32.
[23] A.D. Jagadale, G. Guan, X. Li, X. Du, X. Ma, X. Hao, A. Abudula, Ultrathin nanoflakes of cobalt–manganese layered double hydroxide with high reversibility for asymmetric supercapacitor, J. Power Sources 306 (2016) 526-534.
[24] X. Hao, Z. Jiang, X. Tian, X. Hao, Z.-J. Jiang, Facile Assembly of Co-Ni Layered Double Hydroxide Nanoflakes on Carbon Nitride Coated N-doped Graphene Hollow Spheres with High Electrochemical Capacitive Performance, Electrochim. Acta 253 (2017) 21-30.
[25] J. Liu, J. Wang, B. Zhang, Y. Ruan, L. Lv, X. Ji, K. Xu, L. Miao, J. Jiang, Hierarchical $NiCo_2S_4$@NiFe LDH Heterostructures Supported on Nickel Foam for Enhanced Overall-Water-Splitting Activity, ACS Appl. Mater. Interfaces 9 (2017) 15364-15372.
[26] X. Li, L. Yu, G. Wang, G. Wan, X. Peng, K. Wang, G. Wang, Hierarchical NiAl LDH nanotubes constructed via atomic layer deposition assisted method for high performance supercapacitors, Electrochim. Acta 255 (2017) 15-22.
[27] P.F. Liu, J.J. Zhou, G.C. Li, M.K. Wu, K. Tao, F.Y. Yi, W.N. Zhao, L. Han, A hierarchical NiO/NiMn-layered double hydroxide nanosheet array on Ni foam for high performance supercapacitors, Dalton Trans. 46 (2017) 7388-7391.
[28] W. Guo, C. Yu, S. Li, J. Yang, Z. Liu, C. Zhao, H. Huang, M. Zhang, X. Han, Y. Niu, J. Qiu, High-Stacking-Density, Superior-Roughness LDH Bridged with Vertically Aligned Graphene for High-Performance Asymmetric Supercapacitors, Small 13 (2017) 1701288.
[29] S. K. Singh, V. Dhavale, R. Boukherroub, S. Kurungot, S. Szunerits, N-Doped Porous Reduced Graphene Oxide as an Efficient Electrode Material for High Performance Flexible Solid-State Supercapacitor, Appl. Mater. Today 8 (2017) 141-149.
[30] W. Su, T. Lin, W. Chu, Y. Zhu, J. Li, X. Zhao, Novel synthesis of RGO/NiCoAl–LDH nanosheets on nickel foam for supercapacitors with high capacitance, RSC Adv. 6 (2016) 113123-113131.
[31] X. Jiao, X. Xia, P. Liu, W. Lei, Y. Ouyang, Q. Hao, Nickel cobaltite nanosheets strongly anchored on boron and nitrogen co-doped graphene for high-performance asymmetric supercapacitors, Nanotechnology 28 (2017) 315403.
[32] K. Kakaei, E. Alidoust, G. Ghadimi, Synthesis of N-doped graphene nanosheets and its composite with urea choline chloride ionic liquid as a novel electrode for supercapacitor, J. Alloys Compds. 735 (2018) 1799-1806.
[33] S.K. Singh, V.M. Dhavale, R. Boukherroub, S. Kurungot, S. Szunerits, N-doped porous reduced graphene oxide as an efficient electrode material for high performance flexible solid-state supercapacitor, Appl. Mater. Today 8 (2017) 141-149.
[34] X. Wang, X. Li, X. Du, X. Ma, X. Hao, C. Xue, H. Zhu, S. Li, Controllable Synthesis of NiCo LDH Nanosheets for Fabrication of High-Performance Supercapacitor Electrodes, Electroanalysis 29 (2017) 1286-1293.
[35] G. Nagaraju, G.S. Raju, Y.H. Ko, J.S. Yu, Hierarchical Ni-Co layered double hydroxide nanosheets entrapped on conductive textile fibers: a cost-effective and flexible electrode for high-performance pseudocapacitors, Nanoscale 8 (2016) 812-825.
[36] X. Ma, X. Li, A.D. Jagadale, X. Hao, A. Abudula, G. Guan, Fabrication of $Cu(OH)_2$ @NiFe-layered double hydroxide catalyst array for electrochemical water splitting, Int. J. Hydrogen

Energy 41 (2016) 14553-14561.
[37] X. Yu, M. Zhang, W. Yuan, G. Shi, A high-performance three-dimensional Ni–Fe layered double hydroxide/graphene electrode for water oxidation, J. Mater. Chem. A 3 (2015) 6921-6928.
[38] L. Yu, H. Zhou, J. Sun, F. Qin, F. Yu, J. Bao, Y. Yu, S. Chen, Z. Ren, Cu nanowires shelled with NiFe layered double hydroxide nanosheets as bifunctional electrocatalysts for overall water splitting, Energy Environ. Sci. 10 (2017) 1820-1827.
[39] N. Han, F. Zhao, Y. Li, Ultrathin nickel-iron layered double hydroxide nanosheets intercalated with molybdate anions for electrocatalytic water oxidation, J. Mater. Chem. A 3 (2015) 16348-16353.
[40] C. Andronescu, S. Seisel, P. Wilde, S. Barwe, J. Masa, Y.-T. Chen, E. Ventosa, W. Schuhmann, Influence of temperature and electrolyte concentration on the structure and catalytic oxygen evolution activity of nickel–iron layered double hydroxide, Chem. Eur. J. 24 (2018) 13773-13777.
[41] G. Luo, K. S. Teh, Y. Xia, Z. Li, Y. Luo, L. Zhao, Z. Jiang, Construction of $NiCo_2O_4$@NiFe LDHs core/shell nanowires array on carbon cloth for flexible, high-performance pseudocapacitor electrodes, J. Alloys Compds. 767 (2018) 1126-1132.
[42] Y.-T. Wang, A.-H. Lu, H.-L. Zhang, W.-C. Li, Synthesis of Nanostructured Mesoporous Manganese Oxides with Three-Dimensional Frameworks and Their Application in Supercapacitors, J. Phys. Chem. C 115 (2011) 5413-5421.
[43] Z. Yu, M. McInnis, J. Calderon, S. Seal, L. Zhai, J. Thomas, Functionalized graphene aerogel composites for high-performance asymmetric supercapacitors, Nano Energy 11 (2015) 611-620.
[44] J. Zhu, T. Feng, X. Du, J. Wang, J. Hu, L. Wei, High performance asymmetric supercapacitor based on polypyrrole/graphene composite and its derived nitrogen-doped carbon nano-sheets, J. Power Sources 346 (2017) 120-127.
[45] M. Kuang, T.T. Li, H. Chen, S.M. Zhang, L.L. Zhang, Y.X. Zhang, Hierarchical Cu_2O/CuO/Co_3O_4 core-shell nanowires: synthesis and electrochemical properties, Nanotechnology 26 (2015) 304002.
[46] C. Tang, Z. Tang, H. Gong, Hierarchically Porous Ni-Co Oxide for High Reversibility Asymmetric Full-Cell Supercapacitors, J. Electrochem. Soc. 159 (2012) A651-A656.
[47] Y.-P. Lin, N.-L. Wu, Characterization of $MnFe_2O_4$/$LiMn_2O_4$ aqueous asymmetric supercapacitor, J. Power Sources 196 (2011) 851-854.

Figure captions

Scheme 1. Synthesis of NiFe LDHs/rGO/NF using the electrochemical reduction of GO to rGO and deposition onto NF, followed by electrodeposition of NiFe LDHs.

Figure 1: SEM images of the samples deposited using $Ni(NO_3)_2$•$6H_2O$ and $Fe(NO_3)_3$•$9H_2O$ molar ratios of 5:0 (S_0) (**a**), 1:4 (S_5) (**b**) and 0:5 S_6 (**c**); (**d**) SEM image of NiFe LDHs/rGO/NF (S_7) obtained through electrodeposition using $Ni(NO_3)_2$•$6H_2O$ and $Fe(NO_3)_3$•$9H_2O$ at a molar ratio of 1:4 under constant potential of -1.2 V *vs.* SCE for 10 s.

Figure 2: XPS analysis of NiFe LDH/rGO/NF: (a) Survey spectrum, and high resolution spectra of (b) C_{1s}, (c) Ni_{2p}, and (d) Fe_{2p}.

Figure 3: Electrochemical characteristics of the electrodes upon immersion in 2 M KOH aqueous solution. (a) CV curves recorded at a scan rate of 50 mV s^{-1}. (b) CV curves of NiFe LDH 1:4 at various scan rates. (c) Galvanostatic discharge curves at a current density of 5 A g^{-1}. (d) Specific capacitance at different current densities.

Figure 4: Electrochemical performance of NiFe LDH/NF (S_5) and NiFe LDH/rGO/NF (S_7) electrodes in 2 M KOH aqueous solution. (a) CV curves recorded at a scan rate of 100 mV s^{-1}. (b) CV curves of NiFe LDH/rGO/NF at various scan rates. (c) Galvanostatic discharge curves at a current density of 5 A g^{-1}. (d) Specific capacitance at different current densities. (e) Electrochemical impedance spectra recorded at open circuit potential in the frequency range from 0.01 Hz to 100 kHz. (f) Cycling performance at a constant current density of 15 A g^{-1}.

Figure 5: Electrochemical performance of the NiFe LDH/rGO/NF//MC/NF asymmetric supercapacitor. (a) Schematic diagram of the packed asymmetric supercapacitor device. (b) CV curves performed at different potential windows at 100 mV s^{-1}. (c) CV curves between 0 and +1.5 V recorded at different scan rates. (d) Galvanostatic discharge curves recorded at different current densities. (e) Specific capacitance determined at different current densities. (f) EIS curves in the frequency range of 0.01 Hz and 100 kHz. (g) Ragone plots related to the energy and power densities of the asymmetric supercapacitor. (h) CV curves at recorded at 100 mV s^{-1} upon bending the device at different angles.

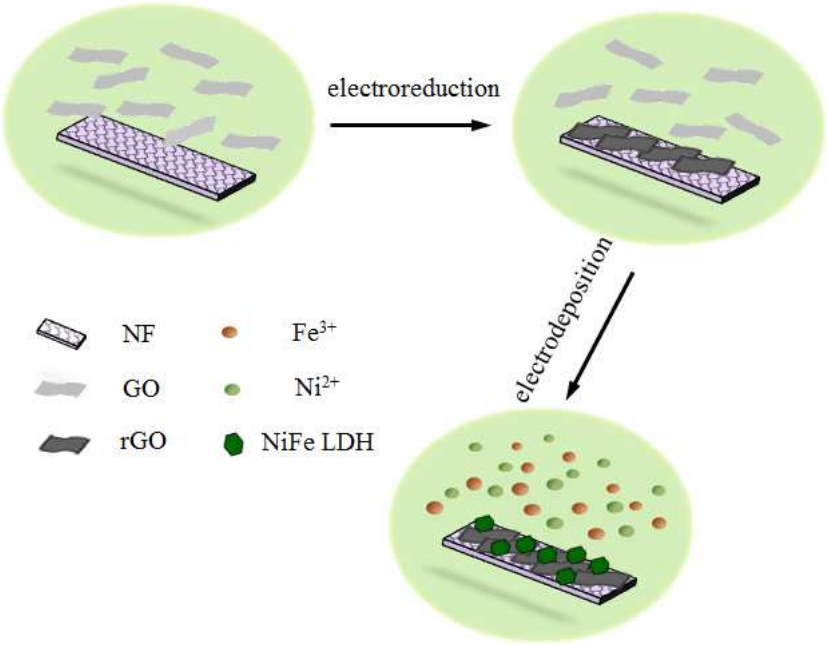
electroreduction
electrodeposition
NF
GO
rGO
Fe3+
Ni2+
NiFe LDH

Scheme 1

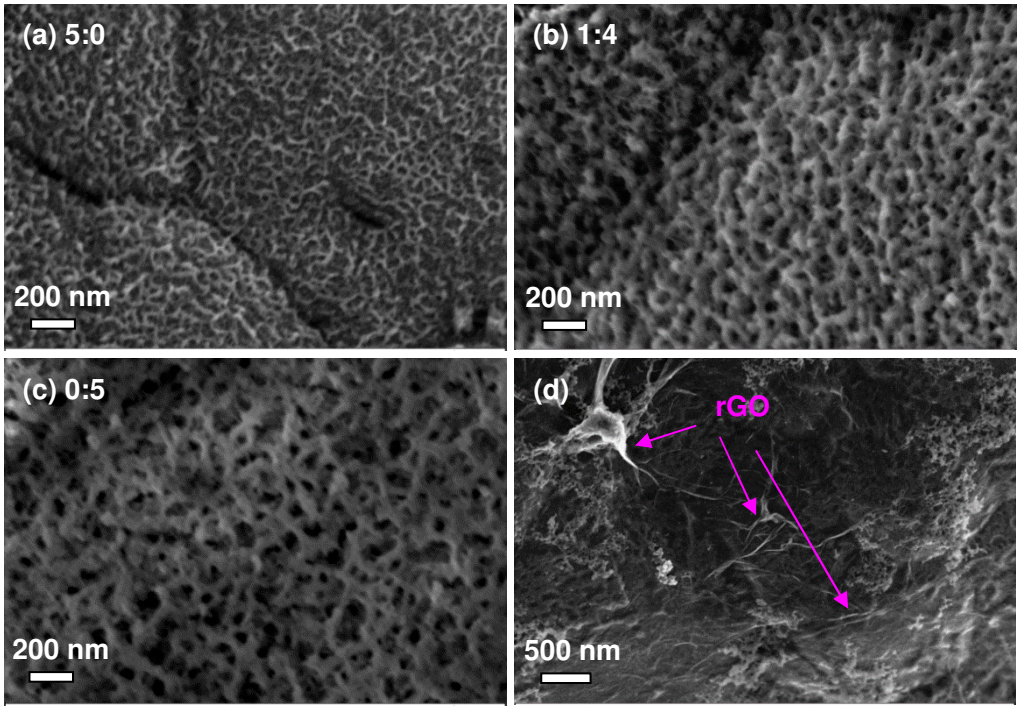

Figure 1

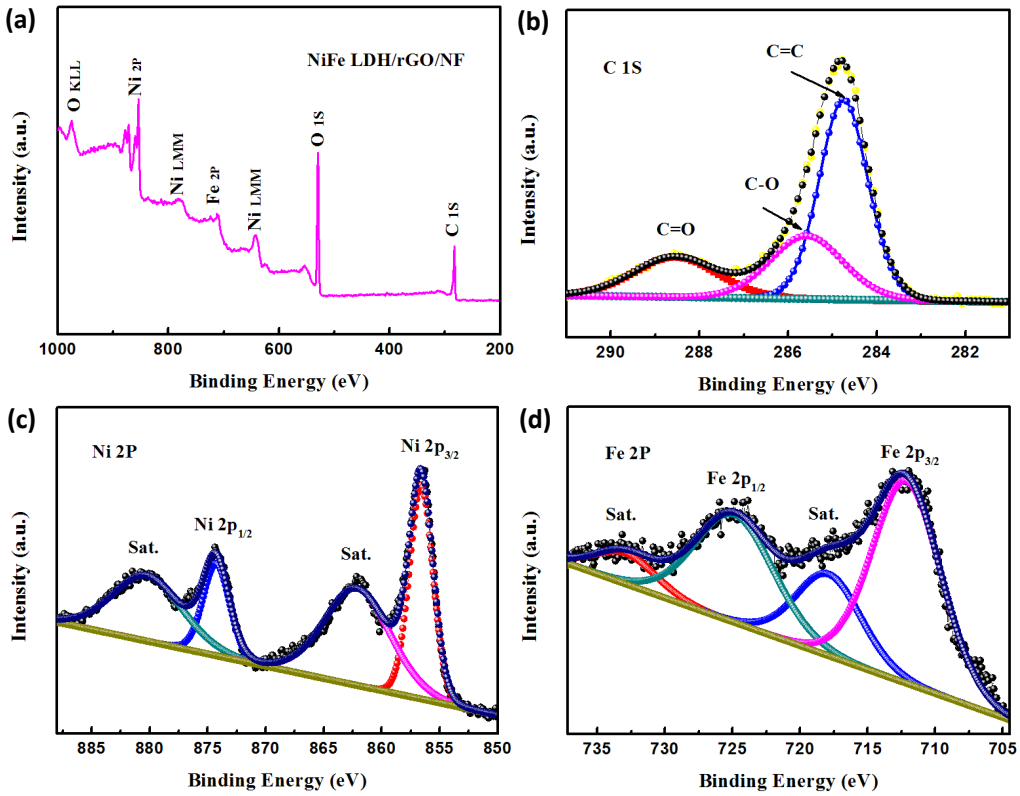
(a)
NiFe LDH/rGO/NF
O KLL
Ni 2P
Ni LMM
Fe 2P
Ni LMM
O 1S
C 1S
Intensity (a.u.)
1000
800
600
400
200
Binding Energy (eV)
(b)
C 1S
C=C
C-O
C=O
Intensity (a.u.)
290
288
286
284
282
Binding Energy (eV)
(c)
Ni 2P
Ni 2p3/2
Ni 2p1/2
Sat.
Sat.
Intensity (a.u.)
885
880
875
870
865
860
855
850
Binding Energy (eV)
(d)
Fe 2P
Fe 2p1/2
Fe 2p3/2
Sat.
Sat.
Intensity (a.u.)
735
730
725
720
715
710
705
Binding Energy (eV)

Figure 2

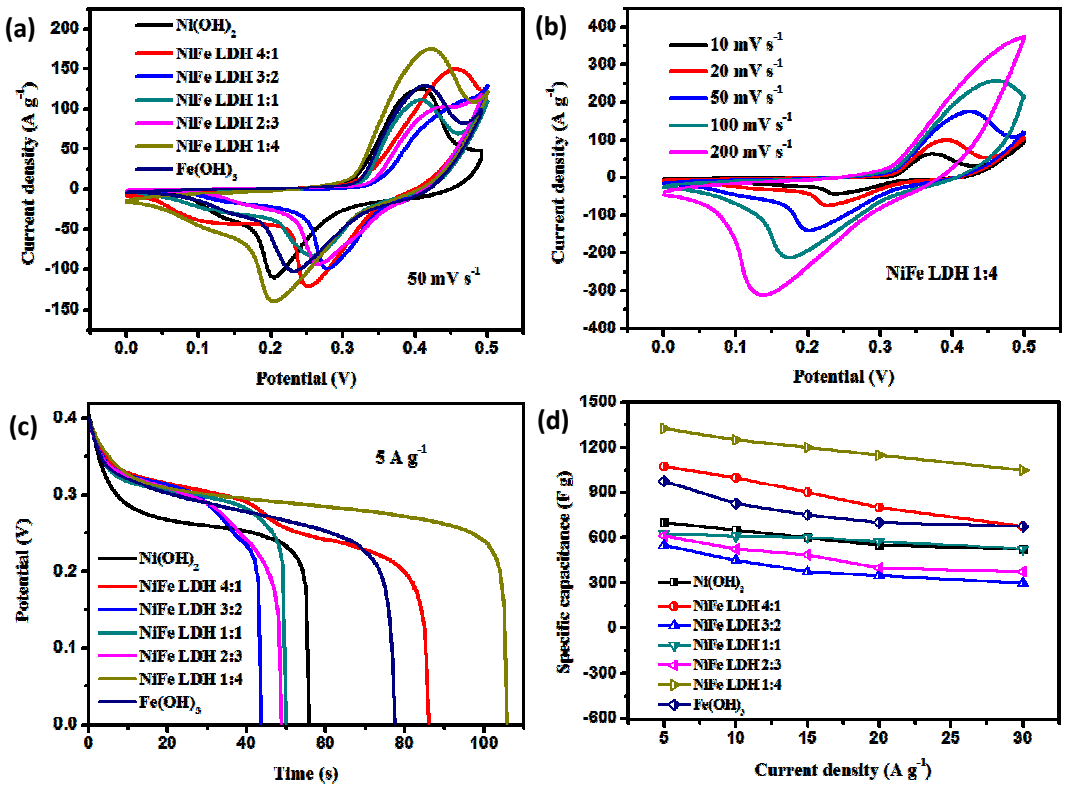
(a)
Ni(OH)2
NiFe LDH 4:1
NiFe LDH 3:2
NiFe LDH 1:1
NiFe LDH 2:3
NiFe LDH 1:4
Fe(OH)3
50 mV s-1
Current density (A g-1)
Potential (V)
(b)
10 mV s-1
20 mV s-1
50 mV s-1
100 mV s-1
200 mV s-1
NiFe LDH 1:4
Current density (A g-1)
Potential (V)
(c)
5 A g-1
Ni(OH)2
NiFe LDH 4:1
NiFe LDH 3:2
NiFe LDH 1:1
NiFe LDH 2:3
NiFe LDH 1:4
Fe(OH)3
Potential (V)
Time (s)
(d)
Ni(OH)2
NiFe LDH 4:1
NiFe LDH 3:2
NiFe LDH 1:1
NiFe LDH 2:3
NiFe LDH 1:4
Fe(OH)3
Specific capacitance (F g)
Current density (A g-1)

Figure 3

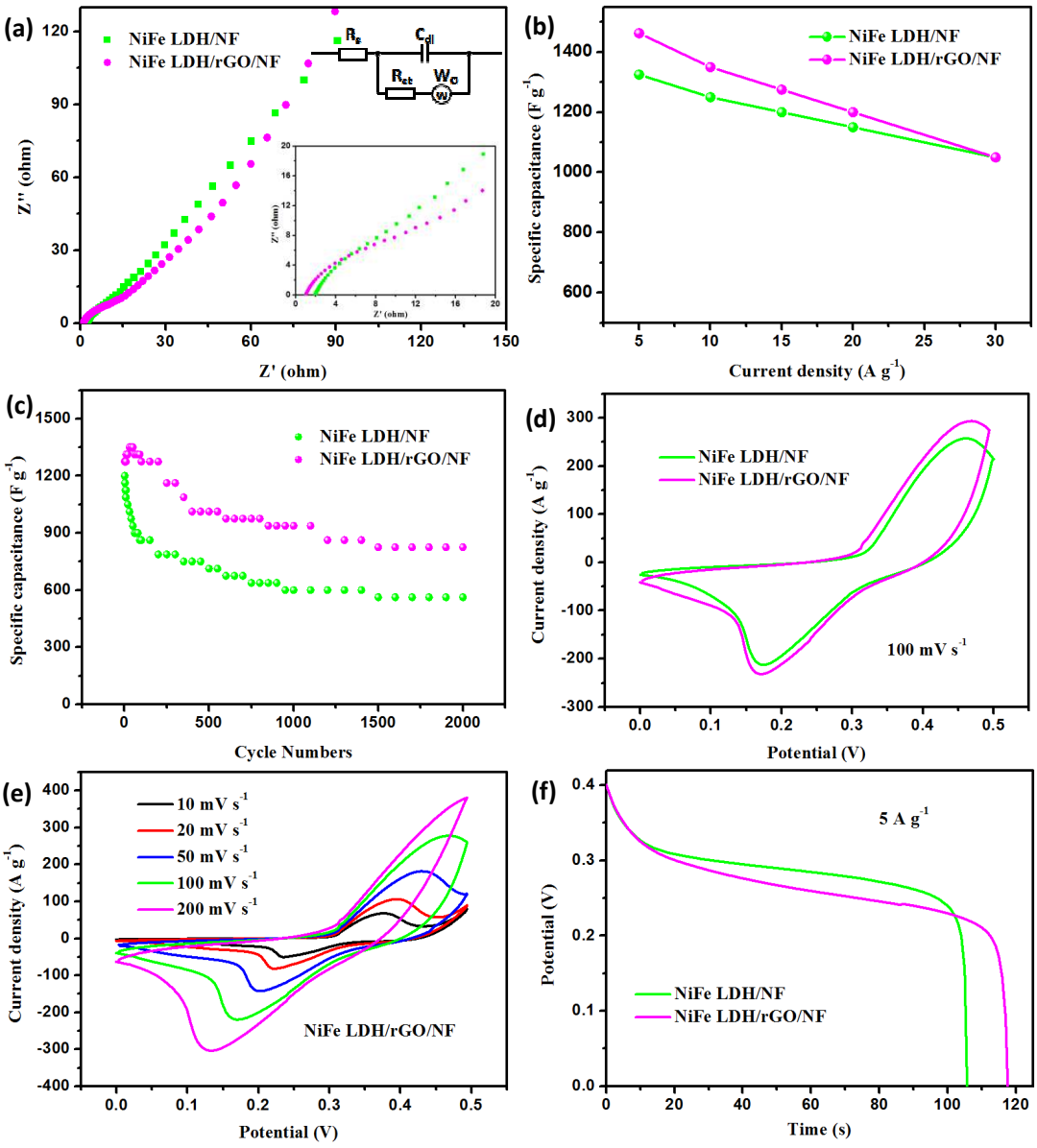
(a)
NiFe LDH/NF
NiFe LDH/rGO/NF
Rs
Cdl
Rct
Wo
Z'' (ohm)
Z' (ohm)
(b)
NiFe LDH/NF
NiFe LDH/rGO/NF
Specific capacitance (F g-1)
Current density (A g-1)
(c)
NiFe LDH/NF
NiFe LDH/rGO/NF
Specific capacitance (F g-1)
Cycle Numbers
(d)
NiFe LDH/NF
NiFe LDH/rGO/NF
100 mV s-1
Current density (A g-1)
Potential (V)
(e)
10 mV s-1
20 mV s-1
50 mV s-1
100 mV s-1
200 mV s-1
NiFe LDH/rGO/NF
Current density (A g-1)
Potential (V)
(f)
5 A g-1
NiFe LDH/NF
NiFe LDH/rGO/NF
Potential (V)
Time (s)

Figure 4

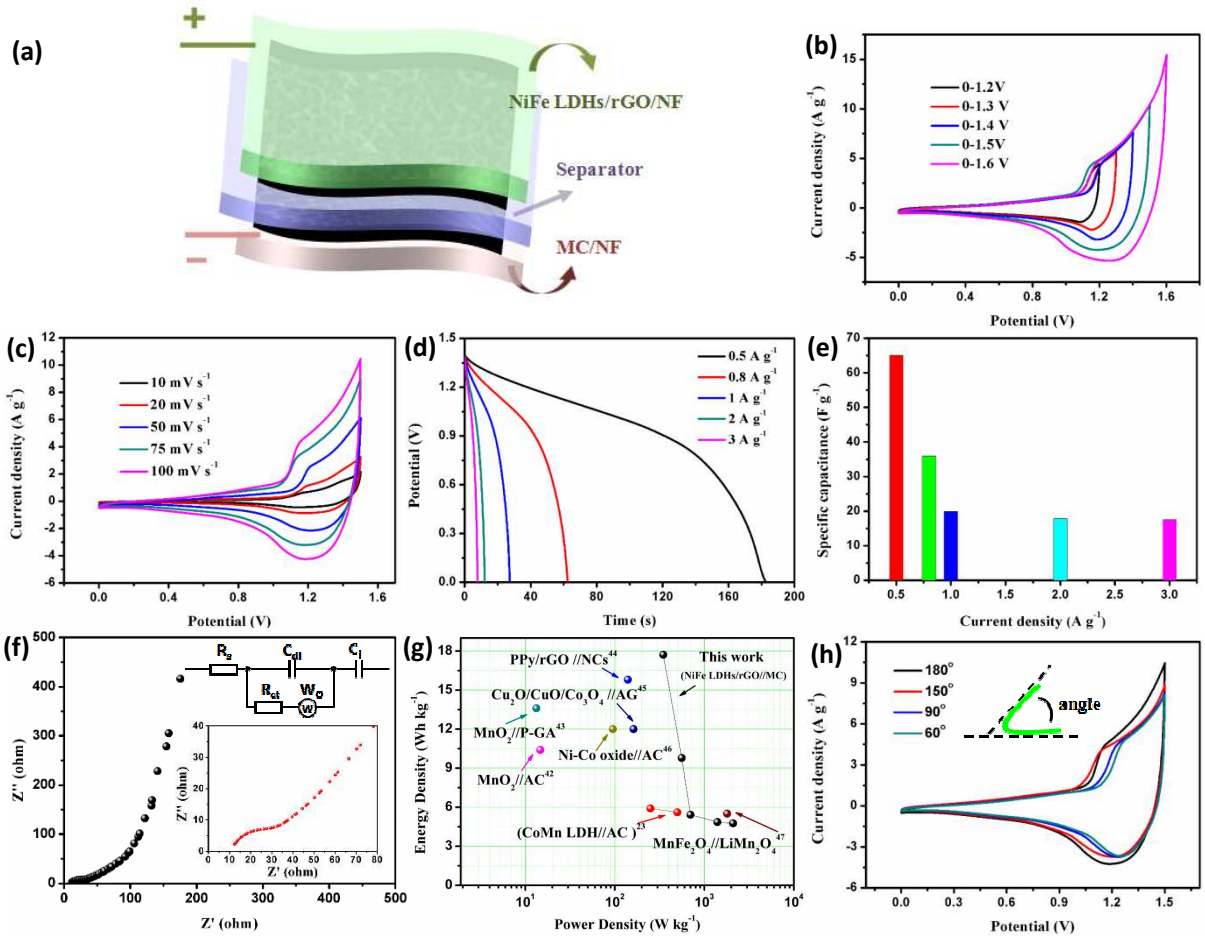
(a)
NiFe LDHs/rGO/NF
Separator
MC/NF
(b)
0-1.2V
0-1.3 V
0-1.4 V
0-1.5V
0-1.6 V
Current density (A g-1)
Potential (V)
(c)
10 mV s-1
20 mV s-1
50 mV s-1
75 mV s-1
100 mV s-1
Current density (A g-1)
Potential (V)
(d)
0.5 A g-1
0.8 A g-1
1 A g-1
2 A g-1
3 A g-1
Potential (V)
Time (s)
(e)
Specific capacitance (F g-1)
Current density (A g-1)
(f)
Rs
Cdl
Ct
Rct
Wo
Z'' (ohm)
Z' (ohm)
(g)
PPy/rGO //NCs44
This work
(NiFe LDHs/rGO//MC)
Cu2O/CuO/Co3O4 //AG45
MnO2//P-GA43
Ni-Co oxide//AC46
MnO2//AC42
(CoMn LDH//AC)23
MnFe2O4//LiMn2O4 47
Energy Density (Wh kg-1)
Power Density (W kg-1)
(h)
180°
150°
90°
60°
angle
Current density (A g-1)
Potential (V)

Figure 5